Electronic supplementary information for

Photocycle of a cyanobacteriochrome: Charge defect on ring *C* impairs conjugation in chromophore

Lisa Köhler,[a] Wolfgang Gärtner,[a] Georgeta Salvan,[b] Jörg Matysik,*[a] Christian Wiebeler,[ac] and Chen Song*[a]

[a]Institut für Analytische Chemie, Universität Leipzig, 04103 Leipzig, Germany.

[b]Institut für Physik, Technische Universität Chemnitz, 09126 Chemnitz, Germany.

[c]Wilhelm-Ostwald-Institut für Physikalische und Theoretische Chemie, Universität Leipzig, 04103 Leipzig, Germany.

*To whom correspondence may be addressed: Jörg Matysik and Chen Song

Email: joerg.matysik@uni-leizpig.de or chen.song@uni-leipzig.de

This PDF file includes:

Experimental

Sample preparation

The protein expression and purification were described elsewhere.[1,2] The preparation of the protein-trehalose amorphous glassy matrices was done on glass petri dishes according to the previous established protocol.[2] In this study, the inverse temperature effect[2,3] which was previously reported for such sugar matrices utilized to stabilize the photocycle intermediates. Initially, a trehalose glass (molar ratio of 20:1 trehalose/protein, T/P) harbouring the pure Pr state was prepared. The dry glassy matrix was then continuously illuminated with light of 650 nm using a 3 W LED (Winger Electronics, Dessau-Roßlau, Germany) for five hours at RT resulting in the formation of the Lumi-R intermediate. For the preparation of the Meta-R intermediate, the Pr TG cooled down to −20 °C and illuminated with 650 nm light for 25 minutes. To trap the intermediates of the reverse reaction, a Pg-state TG with a T/P molar ratio of 50:1 was used. For this purpose, the protein solution was illuminated with 650 nm light for 10 minutes at RT before the addition of trehalose and subjected to drying. The dried glassy matrix was then continuously illuminated with a 530 nm, 3 W Emitter Power LED (Roithner Lasertechnik, Vienna, Austria) for three hours at RT to form the primary intermediate Lumi-G. Subsequently, the late Meta-G intermediate was thermally trapped by cooling the Lumi-G sample to −20 °C. The thermodynamically stable Pr-state sample was obtained by further cooling to −80 °C. After characterization, each TG sample was gently crushed and packed into a 3.2-mm ZrO_2 rotor.

UV-vis absorbance spectroscopy

All measurements were performed on a Shimadzu 1900i spectrophotometer (Shimadzu Deutschland, Duisburg, Germany) equipped with the temperature regulation system TCC-240A. Photoreversibility of Slr1393g3 as solution was confirmed by the irradiation protocol of 650 → 530 → 650 nm using 20 mW LEDs (Roithner Lasertechnik) at 20 °C for two minutes. Moreover, the spectroscopic properties as well as the stability of the trapped photocycle intermediates embedded in TGs were characterized by UV-vis spectroscopy prior to the NMR acquisition.

Solid-state MAS NMR spectroscopy

All MAS experiments were performed on a Bruker AVANCE-III 600 MHz NMR spectrometer (Rheinstetten, Germany) equipped with a 3.2 mm double-resonance MAS probe. The experimental temperature of 25 °C (unless otherwise stated) was maintained with a fluctuation of ± 0.2 °C by a temperature control unit. For both 1D ^{13}C CP and 2D DARR experiments, the MAS rate of 20000 ± 5 Hz was controlled by a Bruker MAS unit. Optimized ^{1}H and ^{13}C $\pi/2$ pulse lengths were 2.3 and 3.5 μs, respectively. ^{13}C transverse magnetization created by ramped CP (100–70%) was transferred from ^{1}H with an optimal contact time of 2 ms. A r.f. lock field of 54.7 kHz was applied on ^{13}C, fulfilling the Hartmann–Hahn condition. During the acquisition, a swept-frequency two-pulse phase modulation heteronuclear decoupling (SW_f-TPPM) at a ^{1}H r.f. field of 113.2 kHz was used for ^{1}H decoupling.[4] For all 1D CP spectra of the protein samples, 24576 scans were accumulated with a relaxation delay time of 2.5 s. A line broadening of 20 Hz and zero-filling to 8192 points were used prior to Fourier transformation.

2D ^{13}C–^{13}C DARR spectra were acquired with a CP contact time of 2 ms and an optimized proton mixing time of 150 ms. In total, 114 t_1-increments were accumulated with 1584 scans in each indirect slice and a relaxation delay of 2 s. The ^{1}H–^{13}C dipolar interaction has been recovered by continuous wave irradiation at r.f. field of 19.1 kHz satisfying the $n = 1$ rotary-resonance condition. During the acquisition a SW_f-TPPM heteronuclear decoupling was applied. A 45° shifted squared sine-bell window function (SSB = 3) and zero-filling to 1024 points was applied to the indirect dimension. A 90° shifted squared sine-bell window function (SSB = 2) was applied in the direct dimension and further zero-filled to 4096 points.

The SUPER[5] data were acquired with a r.f. field of 60.6 kHz for CSA recoupling at a MAS rate of 5000 ± 2 Hz. A total of 24 t_1-increments were recorded with 5120 scans during each of the two γ-integral points with a recycle delay of 2.5 s. A spectral width of 48544 Hz was used. The offset was set to 115 ppm for the ^{13}C channel. All CSA cross-sections from the 2D SUPER experiment were simulated using SIMPSON program.[6] All ^{13}C chemical shifts were referenced to the COO^- signal of solid L-tyrosine·HCl at 172.1 ppm. The data was processed with Bruker Topspin 4.1.3 and further analyzed with MestReNova 14.1.0 (Mestrelab Research, Santiago de Compostella, Spain).

QM/MM optimizations as well as quantum chemical excited state and GIAO calculations

For generating a consistent set of models for the three forms of Slr1393g3, we applied the same simulation protocol for Lumi-G as for Pr and Pg in our previous publication,[7] see the next section for more details. The subsequent QM/MM optimizations with ChemShell[8] in combination with Orca[9] started from the last snapshots of the QM/MM MD simulations to obtain representative structures for the solvated protein in its respective states. Only the conjugated system of the chromophore was chosen as QM region which was described employing the BLYP functional[10,11] and Grimme dispersion correction with Becke-Johnson damping (D3BJ),[12,13] whereas the AMBER14 force field[14] was employed for the rest of the protein and TIP3P[15] for the water molecules. In preliminary optimizations, we employed the def2-SV(P) basis[16] together with the corresponding auxiliary basis for the resolution-of-identity (RI) approximation.[17] For all three forms, around 5000 steps were required to obtain optimized structures. These were further refined with a more accurate QM description by employing cc-pVDZ as basis[18] and not applying the RI approximation leading to convergence in a few dozens of steps.

These models were taken as input geometries for the quantum chemical excited state and GIAO calculations. To obtain reliable results, in particular with respect to the latter, the QM regions consisted of 310 (Pr), 331 (Pg), and 340 (Lumi-G) atoms with the difference being caused by the different number of water molecules that were found in proximity to the chromophore, see Figs. 1, S1, and S4. Moreover, all further atoms up to a distance of 12 Å to any of the QM atoms were included as point charges. The excited state calculations were realized with sTD-DFT[19–21] as implemented in the ORCA software package and they started from CAM-B3LYP[22]/def2-SVP ground state calculations. All excited states up to 10 eV were calculated. This approach was found to be in good agreement with more demanding RI-ADC calculations.[23] These calculations were also the basis for population analysis using the Löwdin scheme. For obtaining the CSA tensors of the carbon and nitrogen atoms, we employed the GIAO method[24] as implemented in Gaussian 16.[25] For this, the B3LYP functional in combination with Jensen's pcSseg-2 basis[26] retrieved from the basis set exchange database[27] was used. For visualization of the principal axis frames of selected atoms, Avogadro[28] was employed.

Protein models and details of simulations for the Lumi-G state

The protein structures of the Pr dark state and the Pg photoproduct were taken from the end of the QM/MM MD trajectories reported in our previous publication.[7] Moreover, we performed similar calculations for Lumi-G. Again, we employed the AMBER software package[29] for setting-up the model. We started from the crystal structure with the PDB code 5M85[30] and the program tleap of the AMBER software was used to automatically assign the protonation states at neutral pH. Only exception was H529, as this His residue was considered to be biprotonated analog to our previous study.[7] We retained the crystallographic water molecules and placed the protein in a rectangular box of TIP3P water molecules[15] with a distance of at least 15 Å between the atoms of the proteins and the boundaries of the box. Seven Na^+ ions were added to neutralize the negatively charged system. The protein was described via the AMBER ff14SB force field.[14] Force field parameters and charges for the PCB chromophore consistent with this force field were taken from our previous work.[31]

During the initial optimizations described here, we employed periodic boundary conditions, a cut-off of 12 Å for non-bonded interactions and the Particle Mesh Ewald method for long-range electrostatics. The optimizations consisted of three stages: *i*) A steepest descent energy minimization with MM was carried out for 100,000 steps, during which only the environment consisting of water molecules and added ions was optimized, whereas harmonic restraints of 500 kcal/(mol $Å^2$) were applied to the rest of the atoms; *ii*) MM optimization with the XMin algorithm, during which restraints were only applied to the SLR residue consisting of the PCB chromophore and C528; this optimization stopped after ca. 5000 steps; and *iii*) QM/MM optimization via 30,000 steps of steepest descent, where the QM region encompassed the C528 sidechain starting with Cβ and PCB; DFTB2+D[32,33] as implemented in the AMBER software[34] was used as efficient QM method.

Also the MD simulations consisted of three stages: *i*) Thermalization of the system to RT with classical MD simulations at constant volume and by increasing the temperature from 0 to 300 K in the first 900 ps followed by 100 ps at constant temperature; *ii*) 100 ns of classical MD simulations at 300 K under constant pressure and with isotropic scaling to allow backbone relaxation (see Fig. S10); and *iii*) 1 ns of DFTB2+D/AMBER MD simulations with a time step of 1 fs and without any restraints. The QM region in this simulation consisted of SLR and the sidechains of H529 and D498 starting with Cβ.

In all MD simulations, a Langevin thermostat[35] with a collision frequency of 1 ps^{-1} was employed and in the latter two stages, a Berendsen barostat[36] with a reference pressure of 1 bar and a pressure relaxation time of 1 ps was used. During the classical MD simulations, harmonic restraints of 10 kcal/(mol $Å^2$) were applied to the atoms of C528 to keep it close to the DFTB2+D/AMBER optimized geometry. In these simulations, we employed the SHAKE algorithm[37,38] allowing time steps of 2 fs and they were performed on GPU.[39–41]

Sidechains included in the QM regions for excited state and GIAO calculations

For both types of calculations for a given form, the same neutral QM region was employed. The QM regions of all forms contained the same atoms of the sidechains from the residues shown in Table S9. Truncation was always carried out between the Cβ and Cα atoms by using hydrogen atoms for capping.

Overview of water molecules in the QM regions

The amount of water molecules included in the QM regions differs between the three forms. For selection of the water molecules, first all such molecules within a distance of a few angstroms relative to any atom of C528 (see Table S9) were visualized. Upon visual inspection, we kept those molecules that either are directly involved in hydrogen bonding with this residue or that are part of a hydrogen bond network around it, see Figs. S1, S2, and S5.

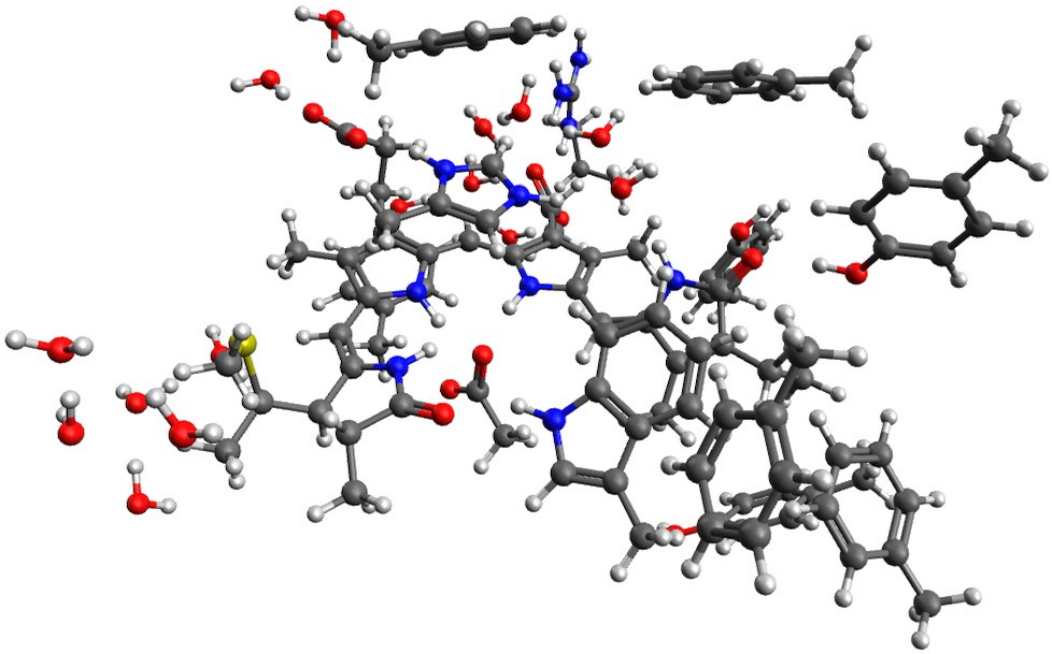

Fig. S1. QM region for the Pr dark state. We selected 14 water molecules in total: six molecules close to the cysteine linkage and the ring ***A***. Two molecules interact with the ***B***-ring propionate sidechain. Six molecules are involved in forming a hydrogen-bonding network between the biprotonated H529 and the ***C***-ring propionate sidechain.

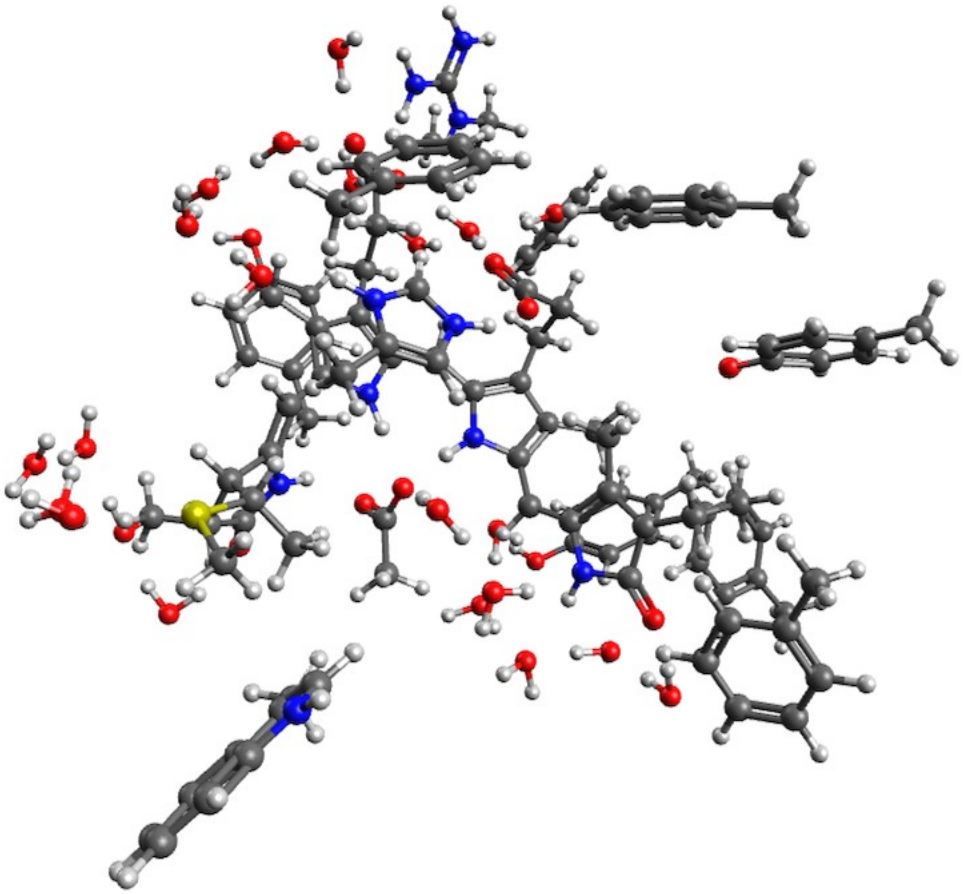

Fig. S2. QM region for the Pg photoproduct. We selected 21 water molecules in total: six molecules close to the cysteine linkage and the ring ***A***; eight molecules forming a hydrogen bond network surrounding the ***B***-ring propionate sidechain and extending to the second propionate; seven molecules forming a hydrogen bond network between D498 and the ring ***D***.

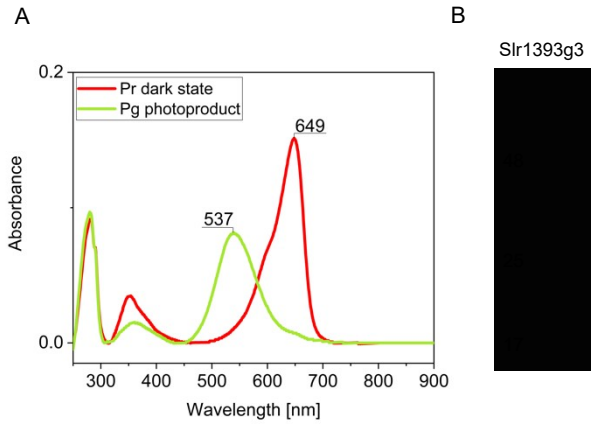

Fig. S3. (A) UV-vis spectra of the CBCR Slr1393g3 in its Pr dark state (red) and Pg photoproduct (green) in solution. The portion of Pr → Pg photoconversion is >95% using the standard illumination protocol described in the methods section. (B) SDS-PAGE of the purified protein. The isolated Slr1393g3 protein has a molecular mass of ~19 kDa.

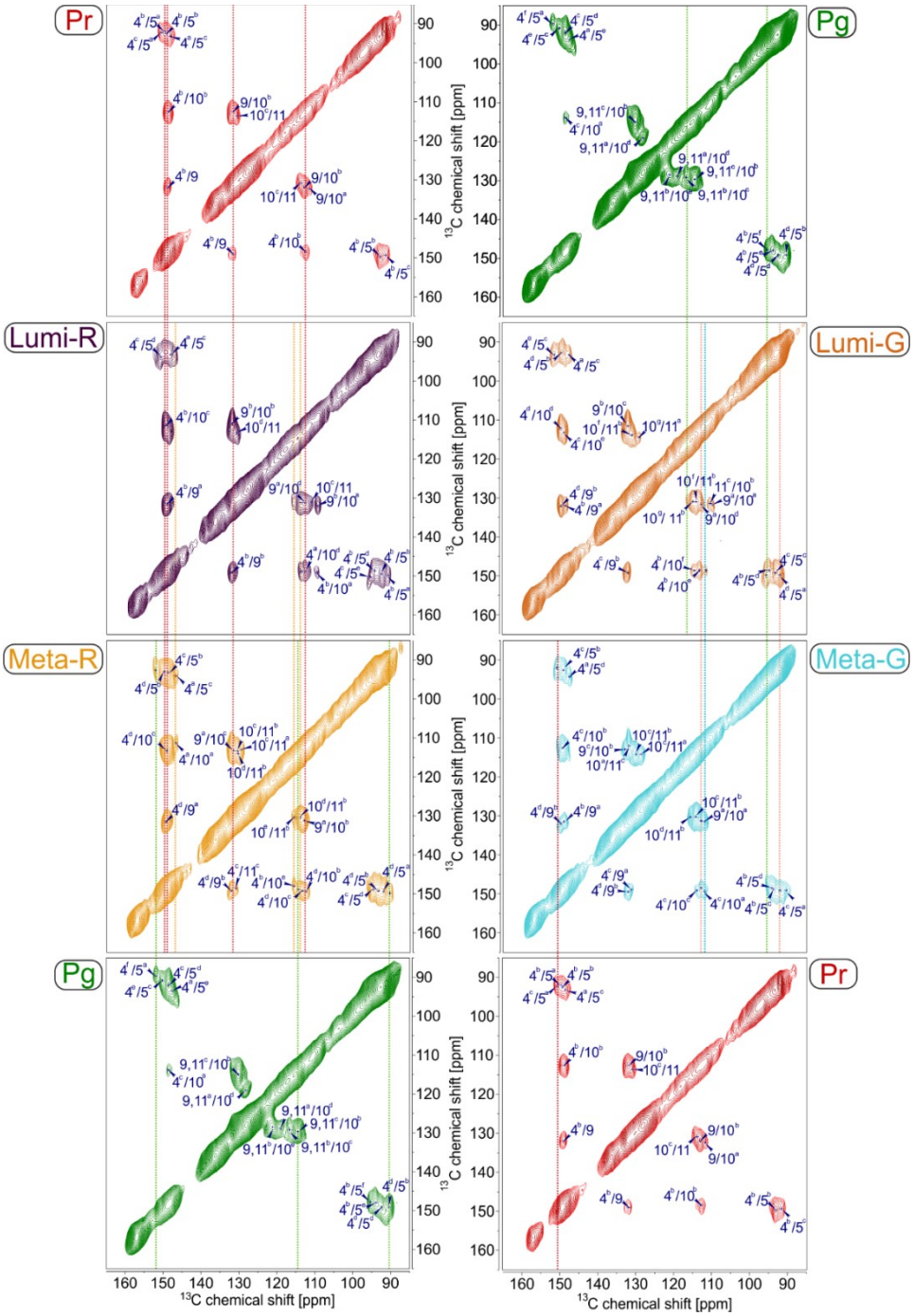

Fig. S4. ^{13}C–^{13}C DARR spectra of the six photocycle states in the Pr → Pg forward-reaction (*left*) and the Pg → Pr backward-reaction (*right*). For a subset of carbons showing multiple chemical shifts, their ^{13}C signals are superscripted with *a*, *b*, *c* and so on from the high- to low-field side.

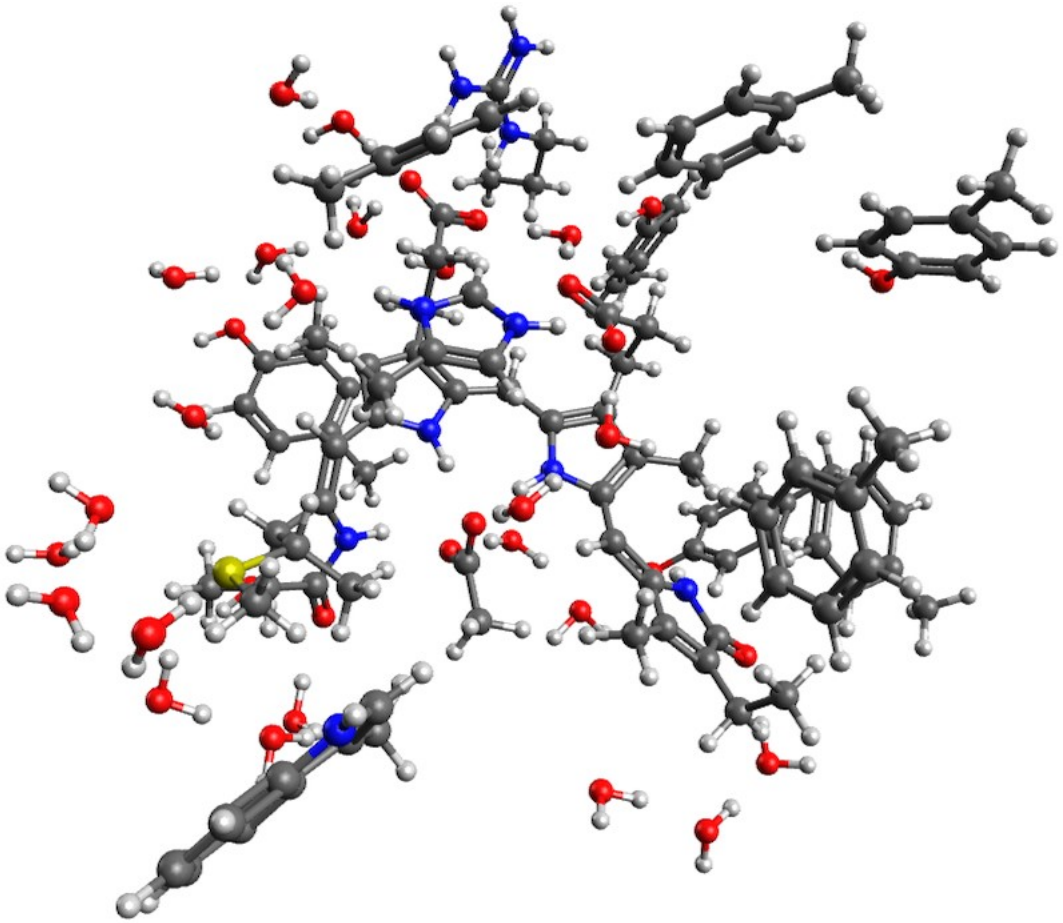

Fig. S5. QM region for the Lumi-G photointermediate. We selected 24 water molecules in total: eight molecules close to the cysteine linkage and the ring ***A***; eight molecules forming a hydrogen bond network surrounding both the ***B***-ring propionate sidechain and the ring itself; one molecule bridging both propionates; two molecules between D498 and the ***C***-ring propionate sidechain; five molecules forming a hydrogen bond network between the second oxygen atom of D498 and ring ***D***.

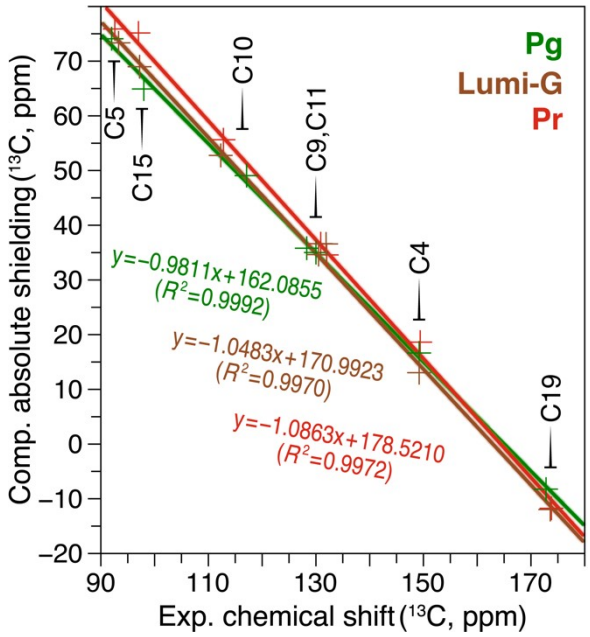

Fig. S6. Plots of the calculated absolute ^{13}C shieldings of all selected PCB carbon atoms versus the experimental chemical shifts in the three photocycle states. For the experimental data, the chemical shift values extracted from the most intense correlation peaks (representing the most populated conformational state, see Fig. S4) were used (summarized in Tables S1 and S3). The equations from linear regression and corresponding R^2 coefficients are inset.

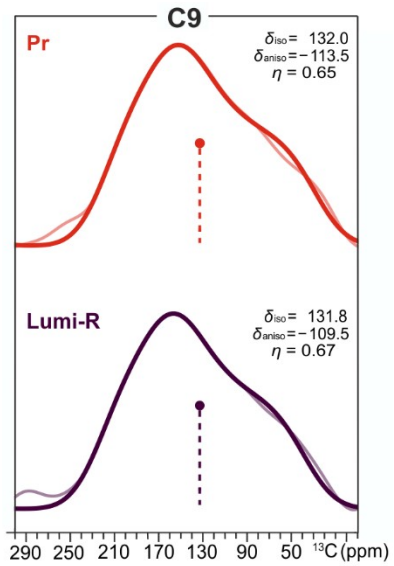

Fig. S7. Cross-sections from the SUPER experiment (thin lines) and simulated CSA lineshapes using SIMPSON (thick lines) of C9 in the Pr state and Lumi-R intermediate. The dashed lines indicate the gravity of the line shape δ_{iso}.

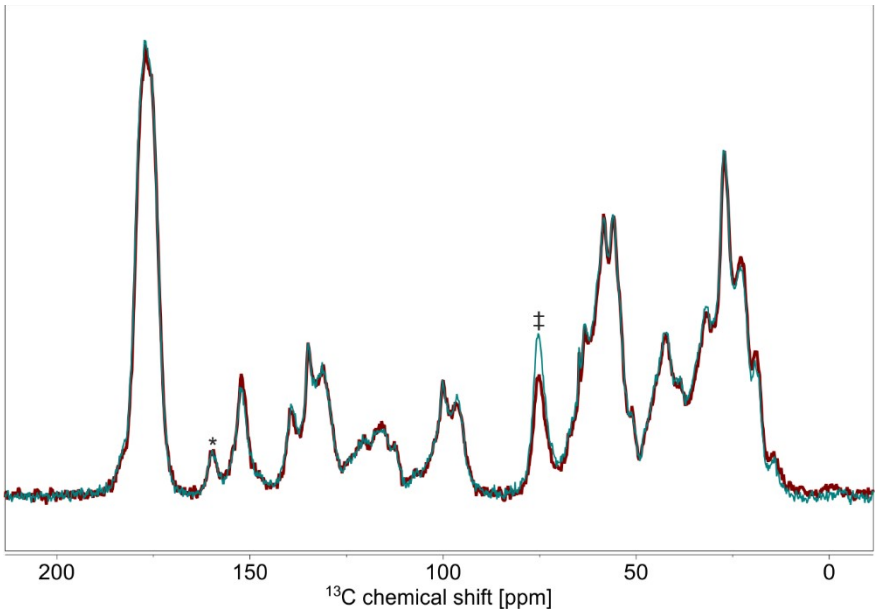

Fig. S8. ^{13}C NMR spectra of freshly prepared Slr1393g3 in its Lumi-R intermediate embedded in the trehalose glassy matrix (brown) and after three-week storage at RT (cyan). The asterisk represents a spinning sideband and the double dagger indicates the signals from trehalose (at 72.5 ppm).

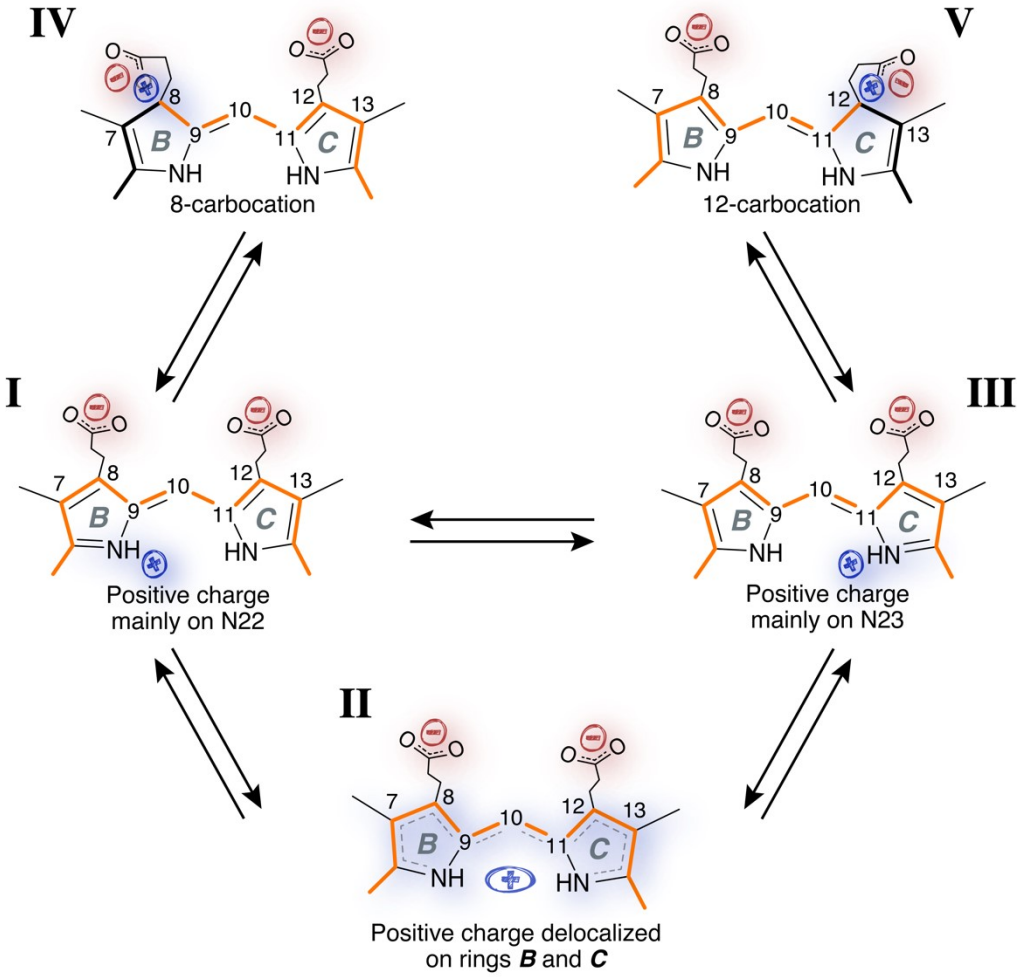

Fig. S9. Possible mesomeric forms of the positively charged chromophore. The formation of stabilized tertiary carbocations at C8 (ring ***B***) and C12 (ring ***C***) impairs the 'core conjugation' formed by the two inner rings ***B*** and ***C*** (colored orange).

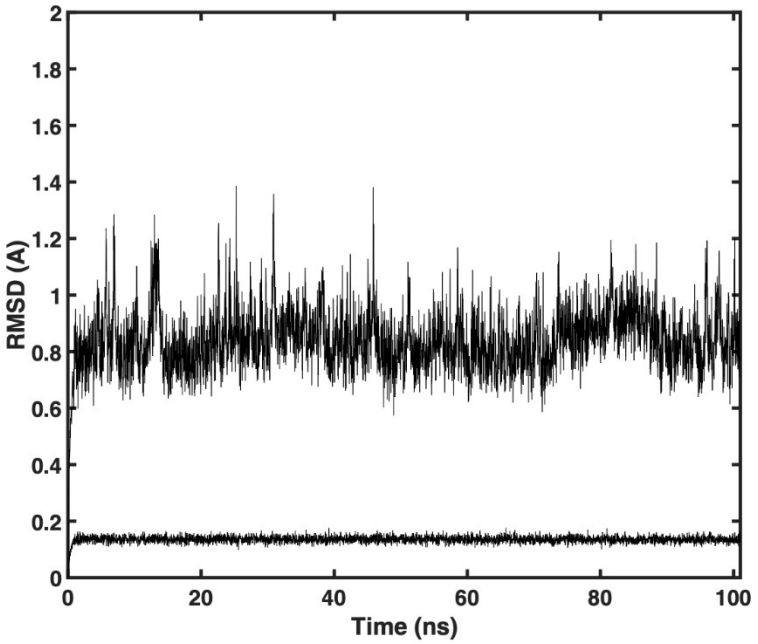

Fig. S10. Root mean square deviation (RMSD, Å) of the backbone atoms (*upper*) and of the restrained C528 residue (*lower*) during the classical MD simulations of the Lumi-G intermediate. The RMSD evaluations of the backbone atoms did not include the first five and the last five amino acids and were realized with CPPTRAJ of the AMBER software. After initial relaxation, the RMSD of the backbone atoms fluctuates in the range between 0.8–1.0 Å, whereas the RMSD of C528 remains below 0.2 Å due to the applied restraints. Both findings are similar to our observations for the Pr dark state and the Pg photoproduct.[7]

Table S1. ^{13}C chemical shifts of selected PCB carbons in Slr1393g3 at various photocycle states. The chemical shift values from the most intense correlation peaks for all selected carbons are colored green and used for comparison of calculated ^{13}C chemical shifts with experimental values as listed in Table S3.

PCB carbons $\Delta\delta^C$ [ppm]			Forward-reaction						Backward-reaction					
			Pr		**Lumi-R**		**Meta-R**		**Pg**		**Lumi-G**		**Meta-G**	
				mean value		mean value		mean value		mean value		mean value		mean value
A	**C4**	*a*	148.2	149.4	148.4	149.6	146.7	148.2	147.3	149.2	147.4	149.2	147.5	148.7
		b	**149.3**		149.5		148.0		148.0		148.6		148.5	
		c	150.8		150.8		148.8		148.6		149.0		149.1	
		d	-		-		149.4		**149.0**		**149.6**		149.6	
		e	-		-		-		149.6		151.4		-	
		f	-		-		-		151.8		-		-	
A–B	**C5**	*a*	92.0	92.6	90.8	93.1	92.2	93.6	89.7	92.0	**92.1**	93.3	90.6	92.8
		b	**92.6**		92.6		93.2		**90.3**		92.7		92.6	
		c	93.2		93.2		93.9		90.9		93.3		93.7	
		d	-		93.8		94.9		92.0		94.9		94.2	
		e	-		95.0		-		93.9		-		-	
		f	-		-		-		95.4		-		-	
B	**C9**	*a*	**132.0**	132.0	131.5	131.8	131.5	131.8	128.1	129.1*	**131.6**	131.9	131.4	132.0
		b	-		132.1		132.1		128.5		132.1		132.0	
		c	-		-		-		**129.7**		-		132.7	
C	**C11**	*a*	**130.9**	130.9	130.6	130.6	129.2	130.2	130.2		129.3	130.4	130.4	131.1
		b	-		-		130.4		-		**130.5**		131.8	
		c	-		-		131.0		-		131.5		-	
B–C	**C10**	*a*	111.5	112.8	109.5	111.0	111.5	113.4	113.8	117.1	110.0	112.3	111.9	113.5
		b	**112.6**		110.0		112.7		**114.5**		110.6		112.6	
		c	114.2		111.5		113.3		116.8		111.5		113.9	
		d	-		112.9		113.9		119.1		**112.1**		115.7	
		e	-		-		115.6		121.1		113.2		-	
		f	-		-		-		-		113.9		-	
		g	-		-		-		-		114.5		-	
C–D	**C15**		**97.0**	-	96.8	-	97.1	-	**98.0**	-	**97.2**	-	96.8	-
D	**C19**		**173.8**	-	173.9	-	173.3	-	**172.8**	-	**173.6**	-	173.8	-

*C9 and C11 cannot be distinguished in the Pg photoproduct state.

Table S2. Correlation integrals of C4–C9 and C4–C10, normalized to the diagonal peak of the protein backbone (20–60 ppm) as a measure of spin-diffusion (SD) efficiency. SD process is distance dependent ($I_{ij} = k/u_{ij}^6$, where I_{ij} is the correlation intensity, k is a proportionality constant and u_{ij} is the distance between the nuclei)[42] and magnetization transfer via dipolar coupling is selected based on the mobility of the carbon atoms and other spin properties.[43] The integral values indicate a more mobile PCB chromophore in the Pg photoproduct, as the distances from C4 to C9 and C10 are only marginally altered upon photoisomerization (distances extracted from the corresponding QM/MM structural models for Pr and Pg).

PCB carbons $\Delta\delta^C$ [ppm]	Forward-reaction			Backward-reaction		
	Pr	**Lumi-R**	**Meta-R**	**Pg**	**Lumi-G**	**Meta-G**
C4–C9	0.009	0.009	0.007	–	0.006	0.006
C4–C10	0.017	0.014	0.016	0.002	0.009	0.011

Table S3. Comparison of experimental and calculated ^{13}C chemical shifts of the selected PCB carbons and their changes between Pr, Pg, and Lumi-G photocycle states (see also Table S1).[†]

	Pr		Lumi-G		Pg	
Atom	**Exp.**	**Calc.**	**Exp.**	**Calc.**	**Exp.**	**Calc.**
C4	149.3	147.2	149.6	150.7	149.0	148.2
C5	92.6	94.5	92.1	93.2	90.3	89.7
C9	132.0	132.5	131.6	128.2	129.7	128.7
C11	130.9	130.6	130.5	130.1	129.7	129.5
C10	112.6	113.1	112.1	112.8	114.5	115.2
C15	97.0	95.2	97.2	97.3	98.0	99.1
C19	173.8	175.2	173.6	174.5	172.8	173.6
	Pg – Pr		**Lumi-G – Pr**		**Lumi-G – Pg**	
Atom	**Exp.**	**Calc.**	**Exp.**	**Calc.**	**Exp.**	**Calc.**
C4	−0.3	1.0	0.3	3.5	0.6	2.5
C5	−2.3	−4.8	−0.5	−1.3	1.8	3.5
C9	−2.3	−3.8	−0.4	−4.3	1.9	−0.5
C11	−1.2	−1.1	−0.4	−0.5	0.8	0.6
C10	1.9	2.1	−0.5	−0.3	−2.4	−2.4
C15	1.0	3.9	0.2	2.1	−0.8	−1.8
C19	−1.0	−1.6	−0.2	−0.7	0.8	0.9

[†]Overall, the changes in chemical shifts of the investigated pyrrolic carbon atoms are relatively small (below 5 ppm). Regarding the differences between Pg and Pr (calculated as Pg – Pr), the changes for C4 are in opposite directions. Besides C4, the changes of other carbons go in the same directions, but deviate easily by a few ppm. Moreover, the calculations tend to overestimate the changes relative to experiments. For the differences between Lumi-G and Pr (as Lumi-G – Pr), the changes found in experiments are below 1 ppm and are mostly overestimated by the calculations, but at least the signs of the changes agree. This also holds for the differences between Lumi-G and Pg (as Lumi-G – Pg), except for C9. In summary, although some of the differences in changes between experimental and calculated values match quite well, deviations in the range of a few ppm are common and a maximum deviation of 3.9 ppm is found for C9 from Lumi-G – Pr. Given the accuracy of the quantum chemical calculations as well as further limitations of our simulations, e.g., no sampling of structures, such differences appear, nonetheless, to be reasonable.

Table S4. Best fits of C9 and C11 cross-sections from the SUPER experiment of the Pr, Lumi-R and Meta-R states. δ_{iso} is the isotropic chemical shift. δ_{aniso} and the dimensionless parameter η represent the reduced anisotropy and the asymmetry of CSA, respectively. The CSA span (Ω) is also provided. The best-fit uncertainties are ±1.2 ppm for δ_{aniso} and ±0.05 for η. Three principal values δ_{11}, δ_{22}, and δ_{33} of the CSA lineshape according to IUPAC nomenclature and the span Ω are given. Due to spectral overlap, only the CSA lineshape for C11 could be obtained for the Meta-R intermediate.

	Pr		**Lumi-R**		**Meta-R**
	C9	C11	C9	C11	C11
δ_{iso} [ppm]	132.0	131.0	131.8	130.6	130.3
δ_{aniso} [ppm]	−113.5	−124.5	−109.5	−111.2	−109.0
η [–]	0.65	0.46	0.67	0.74	0.88
δ_{11} [ppm]	225.6	222.1	223.3	227.3	232.8
δ_{22} [ppm]	151.9	164.4	149.9	145.1	136.9
δ_{33} [ppm]	18.5	6.5	22.3	19.4	21.3
Ω [ppm]	207.1	215.6	200.9	207.9	211.5

Table S5. Calculated isotropic chemical shift δ_{iso}, reduced anisotropy δ_{aniso}, the three principal values δ_{11}, δ_{22}, and δ_{33} as well as the asymmetry (η) and the span (Ω) parameters of C9 and C11 in the Pg photoproduct, Lumi-G intermediate and Pr dark state derived from GIAO calculations. The obtained absolute chemical shieldings were converted into chemical shifts by use of the linear regression functions shown in Fig. S6.

	Pg		**Lumi-G**		**Pr**	
	C9	C11	C9	C11	C9	C11
δ_{iso} [ppm]	129.0	129.8	133.8	135.9	141.0	138.8
δ_{aniso} [ppm]	−80.0	−80.8	−84.6	−89.1	−89.2	−88.7
η [–]	0.42	0.46	0.40	0.39	0.40	0.39
δ_{11} [ppm]	185.8	188.9	193.2	197.6	203.6	200.3
δ_{22} [ppm]	152.1	151.4	159.0	163.2	167.6	166.0
δ_{33} [ppm]	49.0	49.0	49.2	46.8	51.8	50.1
Ω [ppm]	136.8	140.0	144.0	150.9	151.8	150.2

Table S6. Changes of δ_{iso}, δ_{aniso}, the three principal values, and Ω in various transitions of both reaction courses. The values for the forward-reaction are given in Table S4, and those of the backward-reaction are given in Table S5 (see also Fig. 5C).

	Pr → Lumi-R		**Lumi-R → Meta-R**		**Pg → Lumi-G**		**Lumi-G → Pr**	
	C9	C11	C9	C11	C9	C11	C9	C11
δ_{iso} [ppm]	−0.2	−0.4	–	−0.3	+4.8	+6.1	+7.2	+2.9
δ_{aniso} [ppm]	+4.0	+13.3	–	+2.2	−4.6	−8.3	−4.6	+0.4
δ_{11} [ppm]	−2.3	+5.2	–	+5.5	+7.4	+8.7	+10.4	+2.7
δ_{22} [ppm]	−2.0	−19.3	–	−8.1	+6.9	+11.8	+8.6	+2.7
δ_{33} [ppm]	+3.8	+12.9	–	+1.9	+0.2	−2.2	+2.6	+3.3
Ω [ppm]	−6.2	−7.7	–	+3.6	+7.2	+10.9	+7.8	−0.7

Table S7. The in-plane component $\delta_{\text{in-plane}}$ (calculated as $\delta_{11} - \delta_{22}$) for both forward- and backward-reactions.

	C9	C11
Pr	73.7	57.7
Lumi-R	73.4	82.2
Meta-R	–	95.9
Pr → Lumi-R	−0.3	24.5
Lumi-R → Meta-R	–	13.7
Pg	33.7	37.5
Lumi-G	34.2	34.4
Pr	36.0	34.4
Pg → Lumi-G	0.5	−3.1
Lumi-G → Pr	1.8	0

Table S8. Charges of the non-hydrogen atoms from Löwdin population analysis based on the ORCA sTD-DFT calculations for the atoms shown in Fig. S8. The charges for the two carbocations centred at C8 and C12 that might be stabilized by interactions with the charged propionate sidechains are emphasized in bold and the two last lines list the sum of charges from the atoms being part of the pyrrole rings ***B*** or ***C***, respectively.

Atom	Pr	Pg	Lumi-G
C6	0.033	0.021	0.028
C7	−0.085	−0.089	−0.078
C7^{1}	−0.317	−0.325	−0.328
C8	**−0.008**	**−0.011**	**−0.026**
C8^{1}	−0.199	−0.204	−0.203
C8^{2}	−0.249	−0.264	−0.251
C8^{3}	-0.031	0.036	0.019
O8^{3}-1	−0.347	−0.274	−0.266
O8^{3}-2	−0.324	−0.302	−0.293
C9	−0.041	−0.039	−0.040
N22	−0.105	−0.082	−0.087
C10	−0.072	−0.042	−0.051
C11	−0.039	−0.024	−0.024
C12	**−0.005**	**0.012**	**−0.001**
C12^{1}	−0.213	−0.201	−0.199
C12^{2}	−0.245	−0.246	−0.240
C12^{3}	0.018	−0.025	−0.004
O12^{3}-1	−0.300	−0.313	−0.300
O12^{3}-2	−0.319	−0.311	−0.312
C13	−0.066	−0.066	−0.066
C13^{1}	−0.317	−0.318	−0.329
C14	0.056	0.075	0.068
N23	−0.099	−0.085	−0.069
Ring *B*	−0.207	−0.201	−0.202
Ring *C*	−0.154	−0.089	−0.092

Table S9. Residues with sidechains included in the QM region.

Type	Residue	Res (Pr)	Res (Pg)
Y	464	29	24
F	474	39	34
W	496	61	56
D	498	63	58
Y	500	65	60
R	508	73	68
Y	509	74	69
F	525	90	85
SLR[‡]	528	93	88
HIP[§]	529	94	89
F	536	101	96
F	541	106	101
Y	559	124	119

[‡]This residue consists of C528 and the PCB chromophore.
[§]Biprotonated histidine.

References

1 X.-L. Xu, A. Gutt, J. Mechelke, S. Raffelberg, K. Tang, D. Miao, L. Valle, C. D. Borsarelli, K.-H. Zhao and W. Gärtner, *ChemBioChem*, 2014, **15**, 1190–1199.

2 L. Köhler, W. Gärtner, J. Matysik and C. Song, *ChemPhotoChem*, 2022, **6**, e202100220.

3 S. J. Hagen, J. Hofrichter and W. A. Eaton, *Science*, 1995, **269**, 959–962.

4 R. S. Thakur, N. D. Kurur and P. K. Madhu, *Chem. Phys. Lett.*, 2006, **426**, 459–463.

5 S. F. Liu, J. D. Mao and K. Schmidt-Rohr, *J. Magn. Reson.*, 2002, **155**, 15–28.

6 M. Bak, J. T. Rasmussen and N. C. Nielsen, *J. Magn. Reson.*, 2011, **213**, 366–400.

7 C. Wiebeler, A. G. Rao, W. Gärtner and I. Schapiro, *Angew. Chemie Int. Ed.*, 2019, **58**, 1934–1938.

8 S. Metz, J. Kästner, A. A. Sokol, T. W. Keal and P. Sherwood, *Wiley Interdiscip. Rev. Comput. Mol. Sci.*, 2014, **4**, 101–110.

9 F. Neese, *Wiley Interdiscip. Rev. Comput. Mol. Sci.*, 2018, **8**, e1327.

10 A. D. Becke, *Phys. Rev. A*, 1988, **38**, 3098–3100.

11 C. Lee, W. Yang and R. G. Parr, *Phys. Rev. B*, 1988, **37**, 785–789.

12 S. Grimme, J. Antony, S. Ehrlich and H. Krieg, *J. Chem. Phys.*, 2010, **132**, 154104.

13 S. Grimme, S. Ehrlich and L. Goerigk, *J. Comput. Chem.*, 2011, **32**, 1456–1465.

14 J. A. Maier, C. Martinez, K. Kasavajhala, L. Wickstrom, K. E. Hauser and C. Simmerling, *J. Chem. Theory Comput.*, 2015, **11**, 3696–3713.

15 W. L. Jorgensen, *J. Am. Chem. Soc.*, 1981, **103**, 335–340.

16 F. Weigend and R. Ahlrichs, *Phys. Chem. Chem. Phys.*, 2005, **7**, 3297–3305.

17 F. Weigend, *Phys. Chem. Chem. Phys.*, 2006, **8**, 1057–1065.

18 T. H. Dunning, *J. Chem. Phys.*, 1989, **90**, 1007–1023.

19 S. Grimme, *J. Chem. Phys.*, 2013, **138**, 244104.

20 T. Risthaus, A. Hansen and S. Grimme, *Phys. Chem. Chem. Phys.*, 2014, **16**, 14408–14419.

21 C. Bannwarth and S. Grimme, *Comput. Theor. Chem.*, 2014, **1040**–**1041**, 45–53.

22 T. Yanai, D. P. Tew and N. C. Handy, *Chem. Phys. Lett.*, 2004, **393**, 51–57.

23 C. Wiebeler and I. Schapiro, *Molecules*, 2019, **24**, 1720–1744.

24 J. R. Cheeseman, *J. Chem. Phys.*, 1996, **104**, 5497–5509.

25 M. J. Frisch, G. W. Trucks, H. B. Schlegel, G. E. Scuseria, M. A. Robb, J. R. Cheeseman, G. Scalmani, V. Barone, G. A. Petersson, H. Nakatsuji, X. Li, M. Caricato, A. V Marenich, J. Bloino, B. G. Janesko, R. Gomperts, B. Mennucci, H. P. Hratchian, J. V Ortiz, A. F. Izmaylov, J. L. Sonnenberg, D. Williams-Young, F. Ding, F. Lipparini, F. Egidi, J. Goings, B. Peng, A. Petrone, T. Henderson, D. Ranasinghe, V. G. Zakrzewski, J. Gao, N. Rega, G. Zheng, W. Liang, M. Hada, M. Ehara, K. Toyota, R. Fukuda, J. Hasegawa, M. Ishida, T. Nakajima, Y. Honda, O. Kitao, H. Nakai, T. Vreven, K. Throssell, J. A. Montgomery Jr., J. E. Peralta, F. Ogliaro, M. J. Bearpark, J. J. Heyd, E. N. Brothers, K. N. Kudin, V. N. Staroverov, T. A. Keith, R. Kobayashi, J. Normand, K. Raghavachari, A. P. Rendell, J. C. Burant, S. S. Iyengar, J. Tomasi, M. Cossi, J. M. Millam, M. Klene, C. Adamo, R. Cammi, J. W. Ochterski, R. L. Martin, K. Morokuma, O. Farkas, J. B. Foresman and D. J. Fox, Gaussian 16 Revision C.01, 2016.

26 F. Jensen, *J. Chem. Theory Comput.*, 2015, **11**, 132–138.

27 B. P. Pritchard, D. Altarawy, B. Didier, T. D. Gibson and T. L. Windus, *J. Chem. Inf. Model.*, 2019, **59**, 4814–4820.

28 M. D. Hanwell, D. E. Curtis, D. C. Lonie, T. Vandermeerschd, E. Zurek and G. R. Hutchison, *J. Cheminform.*, 2012, **4**, 17.

29 D. A. Case, R. M. Betz, D. S. Cerutti, T. E. Cheatham, III, T. . Darden, R. E. Duke, T. J. Giese, H. Gohlke, A. W. Goetz, N. Homeyer, S. Izadi, P. Janowski, J. Kaus, A. Kovalenko, T. S. Lee, S. LeGrand, P. Li, C. Lin, T. Luchko, R. Luo, B. Madej, D. Mermelstein, K. M. Merz, G. Monard, H. T. Nguyen, H. T. Nguyen, I. Omelyan, A. Onufriev, D. R. Roe, A. Roitberg, C. Sagui, C. L. Simmerling, W. M. Botello-Smith, J. Swails, R. C. Walker, J. Wang, R. M. Wolf, X. Wu, L. Xiao and P. A. Kollmann, AMBER 2016, University of California, San Francisco, 2016.

30 X.-L. Xu, A. Höppner, C. Wiebeler, K.-H. Zhao, I. Schapiro and W. Gärtner, *Proc. Natl. Acad. Sci. U. S. A.*, 2020, **117**, 2432–2440.

31 A. G. Rao, C. Wiebeler, S. Sen, D. S. Cerutti and I. Schapiro, *Phys. Chem. Chem. Phys.*, 2021, **23**, 7359–7367.

32 M. Elstner, D. Porezag, G. Jungnickel, J. Elsner, M. Haugk and T. Frauenheim, *Phys. Rev. B*, 1998, **58**, 7260–7268.

33 M. Elstner, P. Hobza, T. Frauenheim, S. Suhai and E. Kaxiras, *J. Chem. Phys.*, 2001, **114**, 5149–5155.

34 G. D. M. Seabra, R. C. Walker, M. Elstner, D. A. Case and A. E. Roitberg, *J. Phys. Chem. A*, 2007, **111**, 5655–5664.

35 G. S. Grest and K. Kremer, *Phys. Rev. A*, 1986, **33**, 3628–3631.

36 H. J. C. Berendsen, J. P. M. Postma, W. F. Van Gunsteren, A. Dinola and J. R. Haak, *J. Chem. Phys.*, 1984, **81**, 3684–3690.
37 J. P. Ryckaert, G. Ciccotti and H. J. C. Berendsen, *J. Comput. Phys.*, 1977, **23**, 327–341.
38 S. Miyamoto and P. A. Kollman, *J. Comput. Chem.*, 1992, **13**, 952–962.
39 A. W. Götz, M. J. Williamson, D. Xu, D. Poole, S. Le Grand and R. C. Walker, *J. Chem. Theory Comput.*, 2012, **8**, 1542–1555.
40 R. Salomon-Ferrer, A. W. Götz, D. Poole, S. Le Grand and R. C. Walker, *J. Chem. Theory Comput.*, 2013, **9**, 3878–3888.
41 S. Le Grand, A. W. Götz and R. C. Walker, *Comput. Phys. Commun.*, 2013, **184**, 374–380.
42 T. Manolikas, T. Herrmann and B. H. Meier, *J. Am. Chem. Soc.*, 2008, **130**, 3959–3966.
43 D. Huster, X. Yao and M. Hong, *J. Am. Chem. Soc.*, 2002, **124**, 874–883.